Modeling blurring effects due to continuous gantry rotation: Application to region of interest tomography

Jeroen Cant, Willem Jan Palenstijn, Gert Behiels, and Jan Sijbers

Articles you may be interested in

X-ray computed tomography using curvelet sparse regularization
Med. Phys. **42**, 1555 (2015); 10.1118/1.4914368

Spatial resolution of synchrotron x-ray microtomography in high energy range: Effect of x-ray energy and sample-to-detector distance
Appl. Phys. Lett. **101**, 261901 (2012); 10.1063/1.4773239

Speed-of-sound compensated photoacoustic tomography for accurate imaging
Med. Phys. **39**, 7262 (2012); 10.1118/1.4764911

Deblurring of breathing motion artifacts in thoracic PET images by deconvolution methods
Med. Phys. **33**, 3587 (2006); 10.1118/1.2336500

New technique for 2D and 3D X-ray image restoration of pipes in service given a limited access for observation
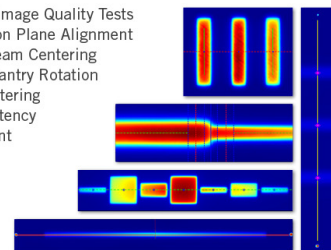AIP Conf. Proc. **557**, 756 (2001); 10.1063/1.1373833

Modeling blurring effects due to continuous gantry rotation: Application to region of interest tomography

Jeroen Cant[a)]
iMinds - Vision Lab, University of Antwerp, B-2610, Antwerp, Belgium and Agfa Healthcare NV, B-2640, Mortsel, Belgium

Willem Jan Palenstijn
iMinds - Vision Lab, University of Antwerp, B-2610, Antwerp, Belgium

Gert Behiels
Agfa Healthcare NV, B-2640, Mortsel, Belgium

Jan Sijbers
iMinds - Vision Lab, University of Antwerp, B-2610, Antwerp, Belgium

Purpose: Projections acquired with continuous gantry rotation may suffer from blurring effects, depending on the rotation speed and the exposure time of each projection. This leads to blurred reconstructions if conventional reconstruction algorithms are applied. In this paper, the authors propose a reconstruction method for fast acquisitions based on a continuously moving and continuously emitting x-ray source. They study the trade-off between total acquisition time and reconstruction quality and compare with conventional reconstructions using projections acquired with a stepwise moving x-ray source.
Methods: The authors introduce the algebraic reconstruction technique with angular integration concept, which models the angular integration due to the relative motion of the x-ray source during the projection.
Results: Compared to conventional reconstruction from projections acquired with pulsed x-ray emission, the proposed method results in substantially improved reconstruction quality around the center of rotation. Outside this region, the proposed method results in improved radial resolution and a decreased tangential resolution. For a fixed reconstruction quality of this region of interest, the proposed method enables a lower number of projections and thus a faster acquisition.
Conclusions: The modeling of the continuous gantry rotation in the proposed method substantially improves the reconstruction quality in a region of interest around the rotation center. The proposed method shows potential for fast region of interest tomography. © *2015 American Association of Physicists in Medicine.* [http://dx.doi.org/10.1118/1.4914422]

Key words: continous scanning, azimuthal blurring, ROI tomography, motion blur, continuous gantry rotation

1. INTRODUCTION

Computed tomography (CT) is increasingly used to study dynamic processes, often referred to as 4D CT. The time resolution with which such processes can be studied strongly depends on the rotation speed of the gantry. Pushing the rotation speed to its limits, however, may result in blurred x-ray projections depending on the type of acquisition, which in turn leads to blurring in the reconstructed images.[1,2]

In a *step-and-shoot* acquisition setup, the x-ray source and detector are stepwise moved on a predefined path and kept still during the exposure.[3] While this approach yields sharp projection images, precisely controlling, moving, and stopping the x-ray source is challenging. As a result, the focal spot often still moves during exposure, which causes blurring in the reconstructed images.[4] In addition, step-and-shoot protocols typically lead to longer acquisition times.[5]

An alternative acquisition strategy is to keep the gantry in a constant motion, a so called *continuous* acquisition mode. This mode allows shorter acquisition times but also suffers from blurred projection data, even if a pulsed x-ray source is employed, as the gantry is still moving during the pulse. A related blurring effect is caused by detector lag, where the detector still partly contains the signal of the previous exposure and hence also appears to store photon beams from multiple angles.[6]

Most acquisition protocols are designed to limit the angular integration as much as possible, either by increasing the detector frame rate,[7,8] by reducing the rotation speed of the gantry, or by decreasing the exposure time of the x-ray pulse.[9,10] Recently, efforts have been made to model the focal spot motion during these x-ray flashes in the reconstruction algorithm to improve the reconstruction quality.[11] Another previous approach to reduce the angular integration consisted of a pixel shifting
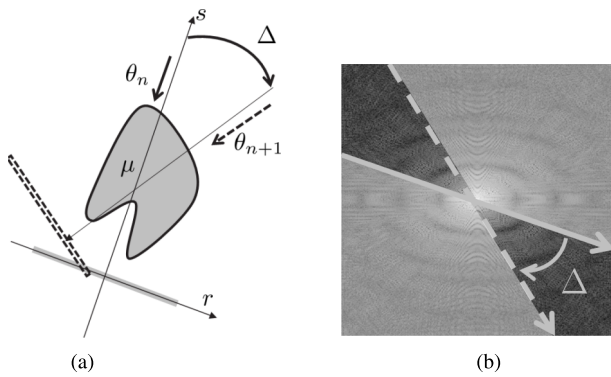
FIG. 1. (a) shows an example image acquisition geometry. Parallel beam projections are acquired at angles $\theta_n = n\Delta$ with $n = 1, \ldots, N$. (b) shows the corresponding lines of these projections in the Fourier space. In a *continuous* acquisition, the detector integrates photons between θ_n and θ_{n+1} and hence gathers information about a wedge of angular width Δ in the Fourier space.

technique.[12] Closely related to angular integration, overlapping beams were modeled originating from multiple sources.[13]

While reducing blurring effects has obvious advantages, the main consequence seems to be prolongation of the acquisition time. An alternative approach, which we will follow in this paper, consists of accurately modeling the blurring effect and integrating it in an image reconstruction framework. Iterative reconstruction methods are known to be suitable to model various physical effects, such as the focal spot size, the beam energy spectrum, and the finite detector elements.[14] In this work, the blurring due to gantry rotation during the acquisition of a single projection is modeled and integrated into a novel acquisition/reconstruction method: the algebraic reconstruction technique with angular integration concept (ARTIC). ARTIC is based on the continuous acquisition mode as described above, but using a continuously emitting x-ray source instead of a pulsed source. The continuously emitting source causes deliberate angular integration of the x-rays along its full motion path from the start of the exposure until the start of the next exposure. Thus, for a given total scan angle, the angle of integration increases with decreasing number of projections. Opposed to conventional reconstruction methods, in ARTIC, the angular integration is modeled and integrated into an iterative reconstruction scheme. The performance of ARTIC in terms of image reconstruction quality is evaluated on simulation phantoms and real datasets.

2. METHODS

2.A. Continuous projections

In this section, we explain the concept of continuous projections for parallel beam geometry. Generalization to other geometries is straightforward. In what follows, a point source and point detector are assumed.

The attenuation of an x-ray beam in the case of a pulsed x-ray source, further referred to as a "static" projection, can be expressed as follows:

$$I_n^s(r) = I_0 \exp\left(-\int_{L_{r,\theta_n}} \mu(x,y)ds\right) \tag{1}$$

with $(x,y) = (r\cos\theta_n - s\sin\theta_n, r\sin\theta_n + s\cos\theta_n)$. Furthermore, I_0 is the intensity measured by the detector without object and I is the intensity after attenuation by the object. The attenuation coefficients of the imaged object are represented by $\mu(x,y)$, and the line integral is taken over the x-ray beam L_{r,θ_n} from source to detector as illustrated in Fig. 1(a).

After transformation of the projection data by $-\ln(I_n^s(r)/I_0)$ and discretization, Eq. (1) can be expressed as a linear combination of the attenuation coefficients

$$b_i = \sum_j a_{i,j}^s x_j, \tag{2}$$

where b_i represents the measured projection data at detector position i and x_j is a pixel in the discrete representation of μ. The contribution of image pixel j to detector value b_i is $a_{i,j}^s$, which is related to the intersection length of the ray with this pixel.

The combination of Eq. (2) for all projection pixels leads to a system of linear equations

$$\mathbf{b} = \mathbf{A^s x}, \tag{3}$$

where $\mathbf{A^s} = \{a_{i,j}^s\}$ represents the system matrix, $\mathbf{x} = \{x_j\}$ represents the vector of unknown attenuation coefficients in the discrete representation of μ, and $\mathbf{b} = \{b_i\}$ represents the vector of the projection data.

In case of continuous projections, each projection value $I_n^c(r)$ is the result of the integration of photons during rotation of the source–detector system from θ_n to $\theta_{n+1} = \theta_n + \Delta$. An equivalent approach can be described with a fixed source–detector system and a continuously rotating object, e.g., in synchrotron imaging. In this case, θ refers to the rotation of the object instead of the source–detector system. If the same total radiation dose is administered and the x-ray source and detector move with constant angular velocity, the measured intensity is given by

$$I_n^c(r) = \frac{I_0}{\Delta} \int_{\alpha=\theta_n}^{\theta_{n+1}} \exp\left(-\int_{L_{r,\alpha}} \mu(x,y)ds\right) d\alpha \tag{4}$$

with $(x,y) = (r\cos\alpha - s\sin\alpha, r\sin\alpha + s\cos\alpha)$. For simplicity, we assume the source emits a constant intensity. Also, the delay for reading out the detector is assumed to be negligible compared to the integration time.

To obtain a discrete formulation of Eq. (4), S number of rays are projected between θ_n and θ_{n+1}. Equation (2) is modified to

$$b_i = -\ln\left(\frac{1}{S}\sum_{s=1}^S \exp\left[-\sum_j a_{i,j,s} x_j\right]\right), \tag{5}$$

where $a_{i,j,s}$ now represents the weight of the attenuation coefficient at image pixel j for the beam arriving at detector pixel i with angle $\theta_n + \frac{s}{S}\Delta$. The sampling factor S should be chosen high enough to sample the full area between the corresponding lines in the Fourier space as illustrated in Fig. 1(b).

Furthermore, under the assumption (see Appendix) that each ray sum $b_{i,s} \equiv \sum_j a_{i,j,s} x_j$ only differs slightly from the average ray sum $b_{i,\text{avg}} \equiv 1/S \sum_{s=1}^S b_{i,s}$, Eq. (5) can be approximated using the fact that $\exp(x) \approx 1 + x$ for small x,

$$b_i = -\ln\left(\frac{1}{S}\sum_{s=1}^{S}\exp(-b_{i,s})\right)$$

$$= -\ln\left(\frac{1}{S}\sum_{s=1}^{S}\exp\left(b_{i,\mathrm{avg}}-b_{i,s}-b_{i,\mathrm{avg}}\right)\right)$$

$$= -\ln\left(\frac{1}{S}\sum_{s=1}^{S}\exp\left(b_{i,\mathrm{avg}}-b_{i,s}\right)\exp\left(-b_{i,\mathrm{avg}}\right)\right)$$

$$= b_{i,\mathrm{avg}} - \ln\left(\frac{1}{S}\sum_{s=1}^{S}\exp\left(b_{i,\mathrm{avg}}-b_{i,s}\right)\right) \tag{6}$$

$$\approx b_{i,\mathrm{avg}} - \ln\left(\frac{1}{S}\sum_{s=1}^{S}\left[1+\left(b_{i,\mathrm{avg}}-b_{i,s}\right)\right]\right)$$

$$= b_{i,\mathrm{avg}}$$

$$= \sum_{j} a^{c}_{i,j} x_j \tag{7}$$

with $a^{c}_{i,j} \equiv 1/S \sum_{s=1}^{S} a_{i,j,s}$.

In this work, we use the linear approximation of Eq. (7) to model the forward continuous projection, which leads to the following linear system:

$$\mathbf{b} = \mathbf{A^c x}, \tag{8}$$

where $\mathbf{A^c} = \{a^{c}_{i,j}\}$ represents the system matrix for the continuous projections.

The linear system in Eq. (8) can then be solved by different techniques. In the remainder of this work, the simultaneous iterative reconstruction algorithm (SIRT) is chosen as an example implementation. In SIRT, the update step can be written as[15]

$$\mathbf{x}^{(k+1)} = \mathbf{x}^{(k)} + \mathbf{C}\mathbf{A}^{T}\mathbf{R}(\mathbf{b}-\mathbf{A}\mathbf{x}^{(k)}) \tag{9}$$

with $\mathbf{A}$ the system matrix, and $\mathbf{R}$ and $\mathbf{C}$ the inverse row and column sums of $\mathbf{A}$, respectively. The reconstructed image in iteration k is represented by $\mathbf{x}^{(k)}$. In this work, we will further refer to "ARTIC" for solving the continuous projections system in Eq. (8) with SIRT, as opposed to "SIRT" for solving the static projections system in Eq. (3) with SIRT.

3. EXPERIMENTS

Section 3.A describes experiments with resolution phantoms. In Sec. 3.B, we describe a simulation experiment using the Forbild[16] phantom. In Sec. 3.C, we perform an experiment on real data, acquired with a synchrotron.

3.A. Resolution phantoms

To compare the reconstruction quality in a region of interest (ROI) between filtered backprojection (FBP),[17] SIRT, and ARTIC, a phantom was created consisting of nonoverlapping randomly placed Gaussian blobs with radius 10 px and a maximal intensity of 1, which decreases to 0 toward the border of the dot [Fig. 2(a)]. The phantom dimensions were 700×700 px. All projections were simulated using parallel beams, with projection angles equally distributed over 180°.

(a) random dots   (b) concentric circles
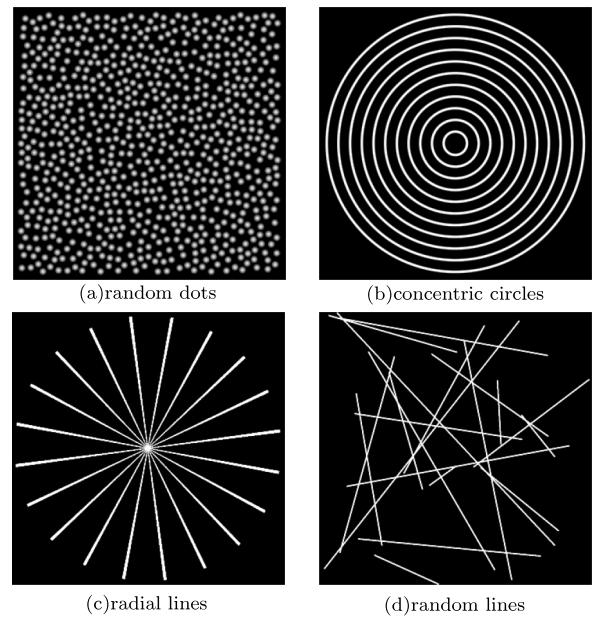
(c) radial lines   (d) random lines

Fig. 2. Phantoms for evaluation of the spatial resolution.

The detector contained 525 elements with a relative pixel width of 2 compared to the phantom pixels. Reconstructions were computed on a grid of size 350×350 px. To measure the reconstruction quality in a ROI, the following local root mean square error (RMSE) was defined:

$$\mathrm{RMSE}(r) \equiv \sqrt{\frac{1}{|D(r)|}\sum_{j\in D(r)}\left(x_j-\widehat{x}_j\right)^2}, \tag{10}$$

where x_j represents the jth pixel of the phantom, $\widehat{x}_j$ is the jth pixel of the reconstructed image, and $D(r)$ is the set of pixels within a circular ROI of relative radius r around the source–detector rotation center, and $|D(r)|$ is its cardinality. A relative radius $r=1$ corresponds to a circular field of view with a radius of half the image width. To exclude differences in convergence speed between both methods, reconstruction iterations were stopped at the iteration at which the reconstructed image showed a minimal RMSE in a ROI of $r=0.5$.

In a first experiment, the relationship between the number of projections and ROI size was investigated. Reconstructions were made using 20, 40, and 60 simulated projections with moderate noise ($I_0 = 10^5$). The RMSE was measured in function of the size of the ROI around the rotation center.

Second, to compare the noise propagation of SIRT and ARTIC through subsequent iterations, three sets of 30 noisy projections with $I_0 = 5\times10^3, 10^4, 10^5$ were simulated. The RMSE of the reconstruction was evaluated in function of the number of iterations in a ROI with radius $r=0.5$.

Third, to illustrate the possible gain in total acquisition time, the RMSE was computed as a function of the number of projections. Moderate noise was added ($I_0 = 10^5$) and both SIRT and ARTIC reconstructions were again stopped at the iteration with minimal RMSE.

The phantom images in Figs. 2(b)–2(d) were designed to illustrate the local radial and angular resolution of ARTIC.
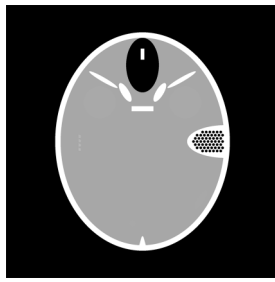
FIG. 3. Forbild phantom.

Pixel intensities are within [0,1]. Phantom dimension, reconstruction grid, detector size, and geometry were identical to the random dots phantom experiments. FBP, SIRT, and ARTIC reconstructions were computed from 20 noiseless projections.

3.B. Anthropomorphic phantom

Simulation experiments were run using the Forbild phantom (Fig. 3). For the simulation of the continuous projections of the anthropomorphic phantoms, Eq. (5) was used to allow validation of the linearization in the reconstruction algorithm in Eq. (7).

The Forbild phantom was generated on a 351×351 pixels grid with pixels of size 75 μm. Projections were simulated with 45 parallel beams, equally distributed over 180°, on a detector of 527 px width to avoid truncation. Moderate noise ($I_0 = 10^5$) was added to the projections. Reconstructions were computed with FBP, SIRT, and ARTIC for different source–detector rotation centers and the RMSE was evaluated around the rotation center for different ROI sizes r. All reconstruction iterations were stopped at the iteration for which the RMSE in a ROI with $r = 0.3$ was minimal.

3.C. Synchrotron measurements

We evaluated our method on two sets of parallel beam projections of an Al8Cu metal rod, made with a synchrotron. The angles of both sets were equally distributed over 180°. The first set consisted of 1000 continuous projections and was considered the reference set. The second set contained only 125 continuous projections.

We reconstructed the set of 1000 projections with SIRT, ignoring the small angular integration, and used it as a reference image. Then, we reconstructed the set of 125 continuous projections with FBP, SIRT, and ARTIC and compared the RMSE with the reference image after rigid registration. We set
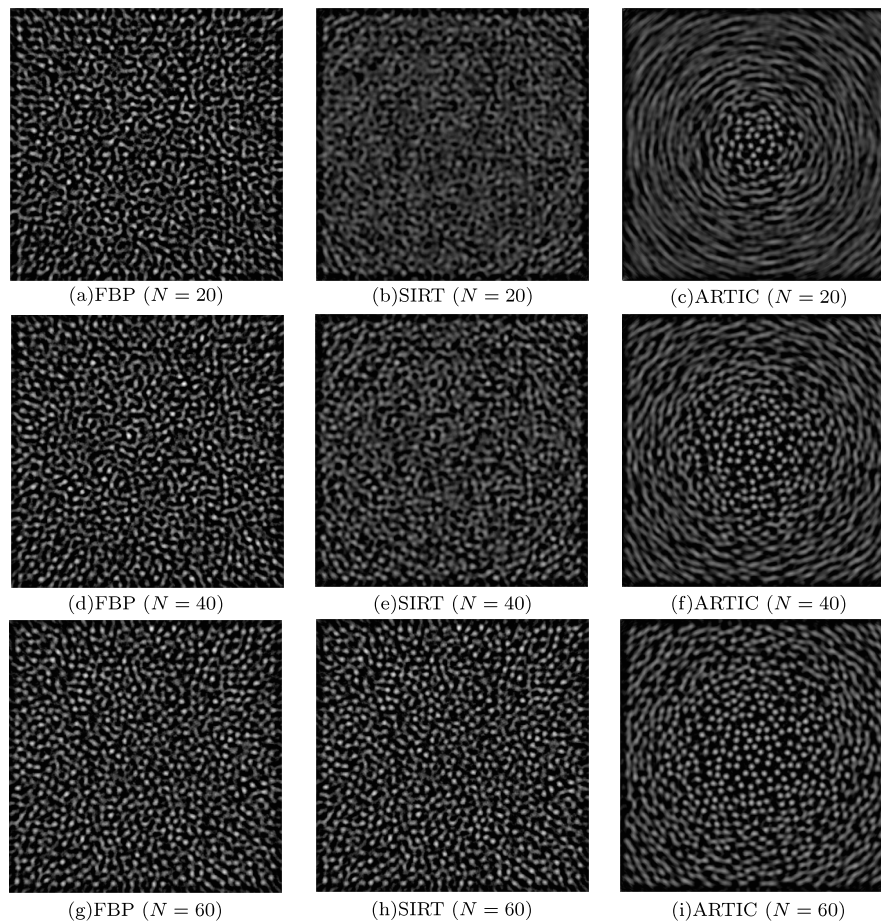

FIG. 4. Reconstructions with FBP (left column), SIRT (middle column), and ARTIC (right column) of the random dots phantom for 20, 40, and 60 projections. Displayed grayscale set to [0,1]. (a) FBP ($N = 20$), (b) SIRT ($N = 20$), (c) ARTIC ($N = 20$), (d) FBP ($N = 40$), (e) SIRT ($N = 40$), (f) ARTIC ($N = 40$), (g) FBP ($N = 60$), (h) SIRT ($N = 60$), (i) ARTIC ($N = 60$).
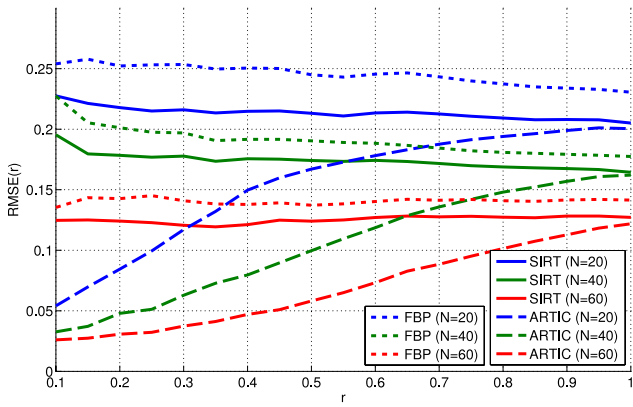
FIG. 5. RMSE in circular ROI with increasing radius r, for various FBP, SIRT, and ARTIC reconstructions of the random dots phantom.

FIG. 7. RMSE ($r = 0.5$) in function of the number of iterations, for various noise levels and $N = 30$.

r to cover the full metal rod excluding the background. We also computed the structural similarity (SSIM)[18] with the reference image for the same region.

4. RESULTS

4.A. Resolution phantoms

Figure 4 shows reconstructions from FBP, SIRT, and ARTIC for an increasing number of projections. Whereas the resolution is not spatially dependent for FBP and SIRT, the results from ARTIC clearly show an improved resolution in a local region around the rotation center, with a decreasing tangential resolution further away from the rotation center. The radius of this local region increases with the number of projections.

Figure 5 shows the RMSE in function of the radius r of the ROI. A substantial improvement is observed with ARTIC for regions with radius $r < 1$. For increasing ROI radius r, the RMSE of SIRT and ARTIC gradually converges toward approximately the same global RMSE. The difference in RMSE between SIRT and ARTIC reconstructions also lowers with increasing number of projections, which can be
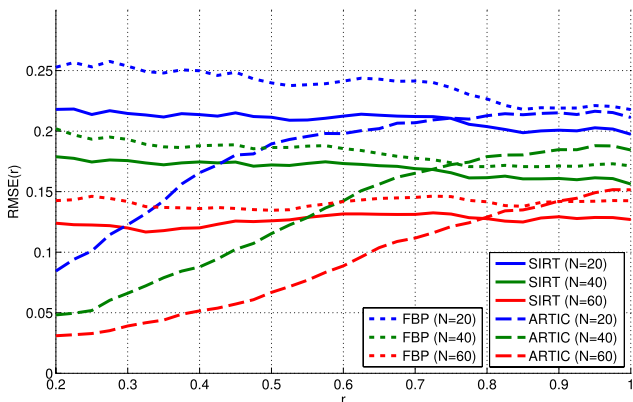
understood intuitively as this reduces the angular integration. To illustrate the spatial dependency of the RMSE in ARTIC reconstructions, Fig. 6 displays the RMSE in a ring of width 0.2 and outer radius r. Around $r = 0.75$ and above, the RMSE of ARTIC is higher than the RMSE of SIRT.

The RMSE of a fixed ROI ($r = 0.5$) in function of the iterations is plotted in Fig. 7 for a fixed number (30) of projections. As can be observed, the RMSE of ARTIC reconstructions increases faster after the optimal stopping iteration compared to SIRT. This illustrates the stronger noise propagation of ARTIC compared to SIRT.

The RMSE in a fixed ROI with radius $r = 0.5$ is displayed in Fig. 8. Note that the RMSE of ARTIC at 30 projections is similar to the RMSE of SIRT at 60 projections, showing its potential for reduction of the scan time.

The reconstructions from projections of the circles phantom [Fig. 9(a)] are displayed in the first row of Fig. 9. Whereas the FBP [Fig. 9(b)] and SIRT reconstructions [Fig. 9(c)] show many artifacts, the ARTIC reconstruction is nearly perfect [Fig. 9(d)]. This demonstrates the improved radial resolution of ARTIC.

The radial lines phantom [Fig. 9(e)] contains lines through the center of rotation and was specifically designed to illustrate

FIG. 6. RMSE in a circular ring of width 0.2 and outer radius r for various FBP, SIRT, and ARTIC reconstructions of the random dots phantom.
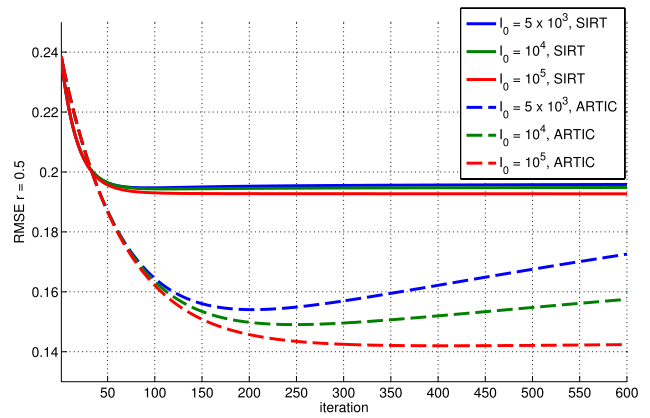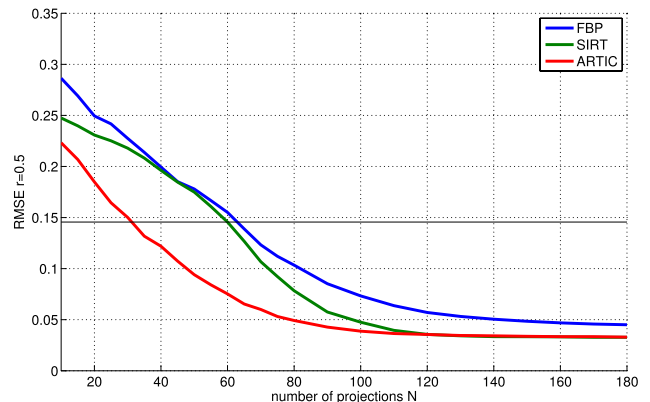

FIG. 8. RMSE ($r = 0.5$) of FBP, SIRT, and ARTIC reconstructions in function of the number of projections.
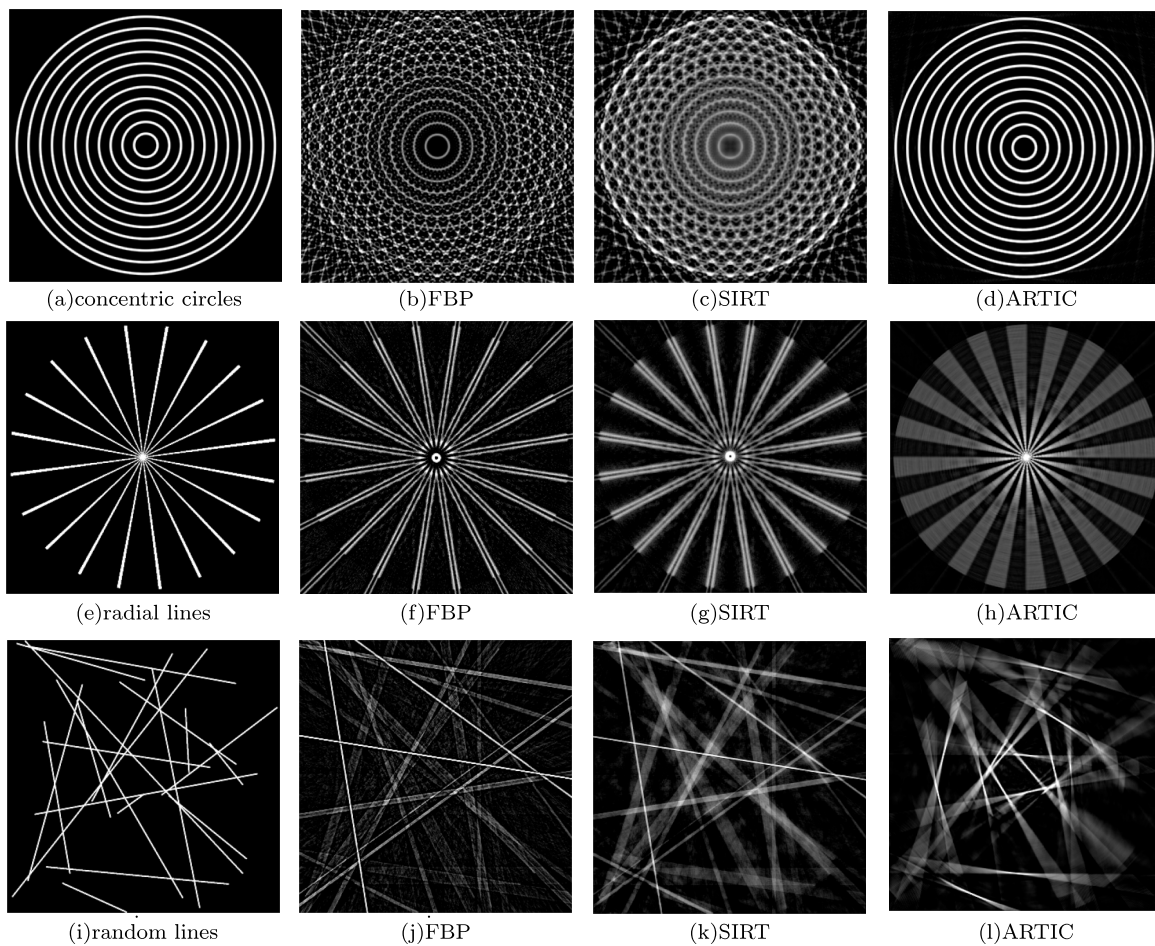
FIG. 9. Reconstructions of the circles phantom (a), radial lines phantom (e), and random lines phantom (i) with FBP, SIRT, and ARTIC. Grayscales displayed at [0,0.5] for increased contrast. $N = 20$ for all reconstructions. (a) Concentric circles, (b) FBP, (c) SIRT, (d) ARTIC, (e) radial lines, (f) FBP, (g) SIRT, (h) ARTIC, (i) random lines, (j) FBP, (k) SIRT, (l) ARTIC.

the decreased tangential resolution of ARTIC. Compared to the FBP [Fig. 9(f)] and SIRT reconstructions [Fig. 9(g)], the ARTIC reconstruction [Fig. 9(h)] shows substantial angular blurring with increasing distance from the rotation center. The angle of this blurring corresponds to the covered angle of the continuous projections. Note that the radial lines phantom illustrates the worst effect of the angular blurring. Figure 9(l) shows the ARTIC reconstruction of a phantom consisting of lines with random orientations [Fig. 9(i)].

4.B. Anthropomorphic phantom

The reconstructions with FBP, SIRT, and ARTIC using two different rotation centers of the Forbild phantom are displayed in Fig. 10. Both SIRT reconstructions had minimal RMSE at 148 iterations, whereas the ARTIC reconstruction iterations stopped at 404 (left) and 1090 (right) iterations. Compared to the FBP [Fig. 10(a)] and SIRT [Fig. 10(c)] reconstructions, the ARTIC reconstruction [Fig. 10(e)] with rotation center in the left of the image shows greater detail and less artifacts in the region around the rotation center. This is reflected in the RMSE, which is displayed in Table I. At the other side of the phantom, the matrix of black holes suffers from angular

blurring. Moving the rotation center to this black holes region on the right improved the result in this region for ARTIC [Figs. 10(f) and 11] but resulted in a smaller improvement compared to FBP [Fig. 10(b)] and SIRT [Fig. 10(d)].

4.C. Synchrotron measurements

The reconstructions with FBP, SIRT, and ARTIC from the synchrotron images are displayed in Fig. 12. The lowest RMSE for SIRT was at 200 iterations and for ARTIC at 400 iterations. Compared to the FBP reconstruction in Fig. 12(a), the ARTIC reconstruction [Fig. 12(c)] shows less noise and a higher contrast in the outer region of the object. In the region close to the rotation center, less differences can be observed. This is due to the relatively high number of 125 projections. The SIRT reconstruction [Fig. 12(b)] shows an overall lower contrast than the ARTIC reconstruction.

Table II shows the quantitative analysis of the reconstructions with the reference image. An improvement is observed for ARTIC, which modeled the relative movement of object and source–detector system during the acquisition of the projections into the reconstruction, compared to FBP and SIRT which ignored the movement.

(a)FBP, left (b)FBP, right

(c)SIRT, left (d)SIRT, right
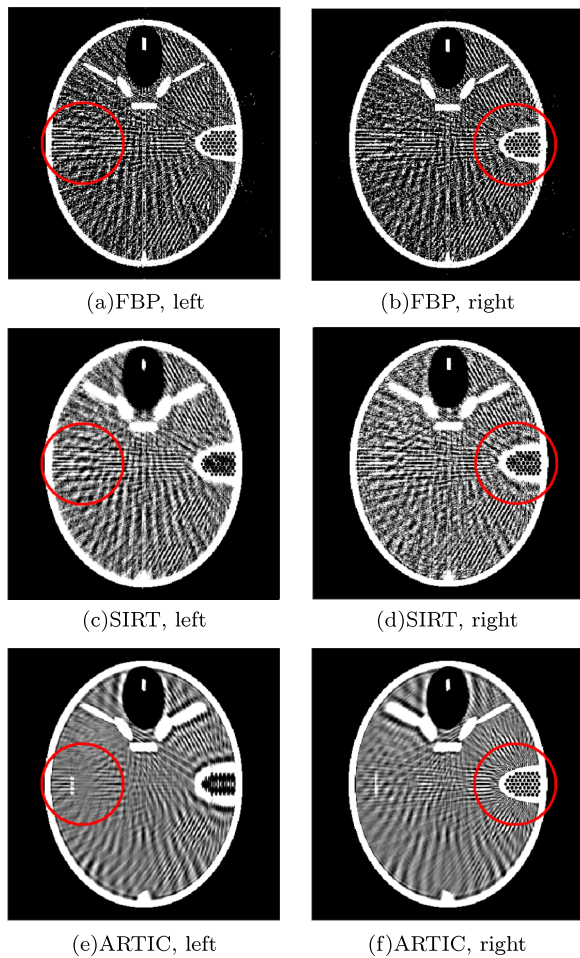
(e)ARTIC, left (f)ARTIC, right

FIG. 10. Reconstructions from 45 projections of the Forbild phantom with rotation center at the left (left column) and right (right column) of the phantom. All images displayed with grayscale [−50,150] HU. The red circle indicates the border of the ROI around the rotation center with radius $r = 0.3$. (a) FBP, left, (b) FBP, right, (c) SIRT, left, (d) SIRT, right, (e) ARTIC, left, (f) ARTIC, right.
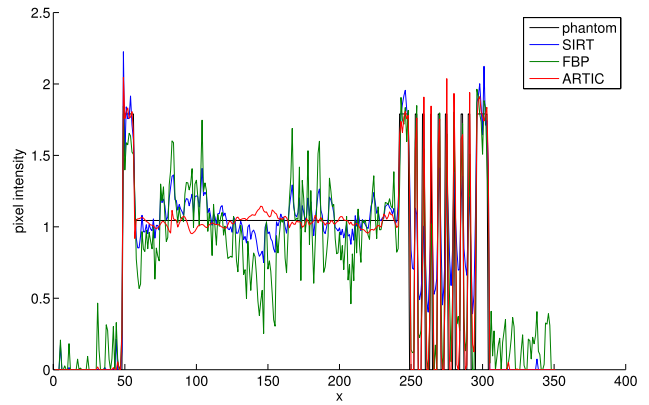

FIG. 11. Profiles through the middle line of FBP, SIRT, and ARTIC reconstructions of the Forbild phantom. Rotation center was in the black holes region on the right of the phantom.

the central slice theorem states that the Fourier transform of a 1D projection of an image corresponds to a line in the Fourier transform of the image.[21] A reconstruction from only a few projections therefore suffers from the well known streak artifacts, due to insufficient information about the Fourier space.

Often applied techniques to deal with few view artifacts are based on compressed sensing, where prior knowledge about the object is incorporated into the reconstruction by a regularization term, which steers the reconstruction toward a more desired result. A typical example of prior knowledge is the assumption that the object can be described by a piecewise constant function, expressed by a low total variation of the image,[22] or a minimal distance to a high resolution prior

5. DISCUSSION

A relatively slow detector that limits the number of projections to maintain temporal resolution can, for example, be found in systems where a flat panel detector is used to capture x-rays[19] from a patient holding his breath. Other examples include synchrotron imagers, where the rotation speed of a sample is limited by the detector read out time.

To avoid reconstruction artifacts, a set of projection images for reconstructing an image should consist of a large number of projections from all angles.[20] For a parallel beam geometry,

TABLE I. Local RMSE for reconstructions of the Forbild phantom with various ROI radii r. Compared to FBP and SIRT, the results for ARTIC (in bold) show a lower RMSE.

	$r = 0.15$			$r = 0.30$		
Rotation center	FBP	SIRT	ARTIC	FBP	SIRT	ARTIC
Left	0.299	0.087	**0.039**	0.279	0.107	**0.061**
Right	0.434	0.518	**0.336**	0.338	0.302	**0.215**

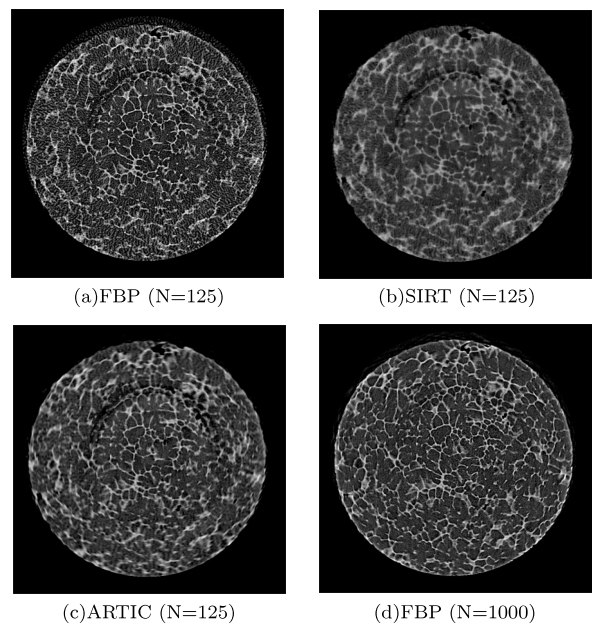(a)FBP (N=125) (b)SIRT (N=125)

(c)ARTIC (N=125) (d)FBP (N=1000)

FIG. 12. Reconstruction of 125 continuous projections of Al8Cu sample using FBP (a), SIRT (b), and ARTIC (c). (d) shows the reference image, reconstructed with FBP for $N = 1000$. All images are displayed at the same grayscale. (a) FBP ($N = 125$), (b) SIRT ($N = 125$), (c) ARTIC ($N = 125$), (d) FBP ($N = 1000$).

TABLE II. RMSE and SSIM for FBP, SIRT, and ARTIC reconstructions of 125 continuous projections of the Al8Cu sample. Compared to FBP and SIRT, ARTIC (in bold) shows a lower RMSE and a higher SSI.

Reconstruction method	RMSE	SSIM
FBP	0.1553	0.7947
SIRT	0.1417	0.7644
ARTIC	**0.1088**	**0.8273**

TABLE III. Average attenuation factors of common tissues in the human body and titanium, as reported by Hubbell and Seltzer (Ref. 25).

Material	$\mu(1/\text{cm})$
Lung tissue	0.2270
Cortical bone	0.4242
Soft tissue	0.2264
Titanium	1.213

reconstruction.[23] In our work, we applied no prior knowledge about the object in the reconstruction other than modeling the continuous acquisition.

In Fig. 1, the nth continuous projection integrates all rays between the angles θ_n and $\theta_n + \Delta$ and thus gathers information from the entire area in the Fourier space between the two angles of the static projections. This reduces the typical streak artifacts caused by reconstructing with too few projections, however at the cost of a decreasing tangential resolution outside the rotation center as discussed in Sec. 4.A. Any form of regularization with prior knowledge could easily be integrated with ARTIC, depending on the type of object being reconstructed.

If detectors are fast enough, distributing the total radiation dose over a high number of $S \times N$ static projections with unattenuated beam intensity I_0/S results in a better overall reconstructed image quality than reconstructing from a few number N continuous projections with beam intensity I_0. In this case, the advantage of ARTIC reduces to a smaller memory footprint of the algorithm on a computing device, as it requires the storage of only a few projection images.

6. CONCLUSION

We propose ARTIC, a reconstruction method for projections that were acquired with a continuously rotating and continuously emitting x-ray source, which causes blurring in the projection images due to the angular integration of the x-ray beams. Compared to conventional reconstruction from a limited number of projections acquired with a pulsed x-ray source, ARTIC improves the resolution in the local neighborhood around the source detector rotation center, at the cost of decreasing tangential resolution further away from this rotation center. Possible applications include region of interest tomography, especially systems where a short total scanning time and a relatively slow detector limit the number of projections that can be acquired.

ACKNOWLEDGMENTS

APPENDIX: LINEARIZATION OF FORWARD PROJECTOR

The linearization of the forward projector in Eq. (7) is based on the assumption that each ray sum $b_{i,s} \equiv \sum_j a_{i,j,s} x_j$ only differs slightly from the average ray sum $b_{i,\text{avg}} \equiv 1/S \sum_{s=1}^{S} b_{i,s}$.

The following example of a cross section of a human thorax illustrates this assumption. We assume a body width of approximately 40 cm and use the attenuation coefficients of Table III. We further assume the x-ray beam is produced by a 100 kV source, which corresponds to an approximate beam energy of 50 keV.[24]

A beam s passing mostly through soft tissue or lung tissue would result in $b_{i,s} \approx \sum_j a_{i,j}^c x_j = 40 \text{ cm} \times 0.2270/\text{cm} = 9.08$. A beam s encountering a lung nodule of 1 cm with an approximate attenuation value of cortical bone results in $b_{i,s} = 9.2772$. If half of the beams contributing to b_i encountered the nodule, this leads to $b_{i,\text{avg}} = 9.1786$. The error made by the linearization is $9.1786 - (-\log((\exp(-9.08) + \exp(-9.2772))/2)) = 0.0049$ or a relative error of 0.0534% on $b_{i,\text{avg}}$.

As a counterexample, assume some of the beams s hit a long structure which is aligned with the beam direction, e.g., a metallic implant of 20 cm length. In this case, $b_{i,s} = 20 \text{ cm} \times 1.213/\text{cm} + 20 \text{ cm} \times 0.2270/\text{cm} = 28.8$, which differs substantially from beams passing only through soft tissue. In this case, the linearization of Eq. (7) would be invalid.

[a]Author to whom correspondence should be addressed. Electronic mail: jeroen.cant2@uantwerpen.be

[1]E. Shaheen, N. Marshall, and H. Bosmans, "Investigation of the effect of tube motion in breast tomosynthesis: Continuous or step and shoot?," Proc. SPIE **7961**, 79611E (2011).

[2]D. Tack, M. Kalra, and P. Gevenois, "Radiation dose from multidetector CT," *Medical Radiology* (Springer, Berlin, Heidelberg, 2012), pp. 87–88.

[3]J. Hsieh, J. Londt, M. Vass, J. Li, X. Tang, and D. Okerlund, "Step-and-shoot data acquisition and reconstruction for cardiac x-ray computed tomography," Med. Phys. **33**, 4236–4248 (2006).

[4]J.-J. Sonke, B. Brand, and M. van Herk, "Focal spot motion of linear accelerators and its effect on portal image analysis," Med. Phys. **30**, 1067–1075 (2003).

[5]A. Smith, "Fundamentals of breast tomosynthesis," White Paper, WP-00007, Hologic Inc., 2008, available at http://www.breasttomo.com/sites/breasttomo.com/files/011-WP-00007_Tomo_08-08.pdf.

[6]J. Baek and N. J. Pelc, "Effect of detector lag on CT noise power spectra," Med. Phys. **38**, 2995–3005 (2011).

[7] W. A. Kalender, W. Seissler, and P. Vock, "Single-breath-hold spiral volumetric CT by continuous patient translation and scanner rotation," Radiology **176**, 181–183 (1990).

[8] W. A. Kalender, "X-ray computed tomography," Phys. Med. Biol. **51**, R29–R43 (2006).

[9] N. W. Marshall and H. Bosmans, "Measurements of system sharpness for two digital breast tomosynthesis systems," Phys. Med. Biol. **57**, 7629–7650 (2012).

[10] H. U. Kerl, C. T. Isaza, H. Boll, S. J. Schambach, I. S. Nolte, C. Groden, and M. A. Brockmann, "Evaluation of a continuous-rotation, high-speed scanning protocol for micro-computed tomography," J. Comput. Assisted Tomogr. **35**, 517–523 (2011).

[11] K. Michielsen, K. Van Slambrouck, A. Jerebko, and J. Nuyts, "Patchwork reconstruction with resolution modeling for digital breast tomosynthesis," Med. Phys. **40**(3), 031105 (10pp.) (2013).

[12] T. Nowak, M. Hupfer, F. Althoff, R. Brauweiler, F. Eisa, C. Steiding, and W. A. Kalender, "Time-delayed summation as a means of improving resolution on fast rotating computed tomography systems," Med. Phys. **39**, 2249–2260 (2012).

[13] D. Yu, J. Fessler, and E. Ficaro, "Maximum-likelihood transmission image reconstruction for overlapping transmission beams," IEEE Trans. Med. Imaging **19**, 1094–1105 (2000).

[14] J. Nuyts and B. De Man, "Modelling the physics in the iterative reconstruction for transmission computed tomography," Phys. Med. Biol. **58**, R63–R96 (2013).

[15] J. Gregor and T. Benson, "Computational analysis and improvement of SIRT," IEEE Trans. Med. Imaging **27**, 918–924 (2008).

[16] Z. Yu, F. Noo, F. Dennerlein, A. Wunderlich, G. Lauritsch, and J. Hornegger, "Simulation tools for two-dimensional experiments in x-ray computed tomography using the forbild head phantom," Phys. Med. Biol. **57**, N237–N252 (2012).

[17] L. Feldkamp, L. Davis, and J. Kress, "Practical cone-beam algorithm," J. Opt. Soc. Am. A **1**, 612–619 (1984).

[18] Z. Wang, A. C. Bovik, H. R. Sheikh, and E. P. Simoncelli, "Image quality assessment: From error visibility to structural similarity," IEEE Trans. Image Process. **13**, 600–612 (2004).

[19] D. A. Jaffray and J. H. Siewerdsen, "Cone-beam computed tomography with a flat-panel imager: Initial performance characterization," Med. Phys. **27**, 1311–1323 (2000).

[20] B. Smith, "Image reconstruction from cone-beam projections: Necessary and sufficient conditions and reconstruction methods," IEEE Trans. Med. Imaging **4**, 14–25 (1985).

[21] R. N. Bracewell, "Strip integration in radio astronomy," Aust. J. Phys. **9**, 198–217 (1956).

[22] E. Y. Sidky, C.-M. Kao, and X. Pan, "Accurate image reconstruction from few-views and limited-angle data in divergent-beam CT," J. Xray Sci. Technol. **14**, 119–139 (2006), see http://iospress.metapress.com/content/1JDUV1CLL3F9E2BR.

[23] G.-H. Chen, J. Tang, and S. Leng, "Prior image constrained compressed sensing (PICCS): A method to accurately reconstruct dynamic CT images from highly undersampled projection data sets," Med. Phys. **35**, 660–663 (2008).

[24] W. Huda, E. M. Scalzetti, and G. Levin, "Technique factors and image quality as functions of patient weight at abdominal CT," Radiology **217**, 430–435 (2000).

[25] J. H. Hubbell and S. M. Seltzer, "Tables of x-ray mass attenuation coefficients and mass energy-absorption coefficients," NISTIR 5632, National Institute of Standards and Technology, Gaithersburg, MD (1995), available at http://physics.nist.gov/xaamdi.

[26] W. Palenstijn, K. Batenburg, and J. Sijbers, "Performance improvements for iterative electron tomography reconstruction using graphics processing units (GPUs)," J. Struct. Biol. **176**, 250–253 (2011).

[27] W. J. Palenstijn, K. J. Batenburg, and J. Sijbers, "The ASTRA tomography toolbox," in *13th International Conference on Computational and Mathematical Methods in Science and Engineering, CMMSE 2013* (Almeria, Spain, 2013), Vol. 4, pp. 1139–1145.